

Article

# Model Test and Numerical Study on Surrounding Rock Deformation and Overburden Strata Movement Law of Gob-Side Entry Retaining via Roof Cutting

Daoyong Zhu <sup>1,2</sup> , Jiong Wang <sup>1,2,\*</sup>, Weili Gong <sup>1,2</sup> and Zheng Sun <sup>1,2</sup>

<sup>1</sup> School of Mechanics and Civil Engineering, China University of Mining & Technology, Beijing 100083, China; zdy@student.cumtb.edu.cn (D.Z.); gwl@cumtb.edu.cn (W.G.); zqt1800601014g@student.cumtb.edu.cn (Z.S.)

<sup>2</sup> State Key Laboratory for Geomechanics & Deep Underground Engineering, China University of Mining & Technology, Beijing 100083, China

\* Correspondence: wangjiong0216@163.com

Received: 13 April 2020; Accepted: 14 May 2020; Published: 19 May 2020



**Abstract:** The effects of roof cutting techniques on the movement law of the overlying strata and deformation features of the surrounding rock in gob-side entry retaining mines were studied using 200 working faces of the Dianping coal mine in Shanxi Province. Using a mechanical analysis, a cantilever beam model formed by roof cutting was used to derive a deformation equation. The physical model test based on the field prototype revealed an asymmetrically distributed displacement curve and reduced collapse displacement when the rock stratum was far from the cutting seam. Outside of the roof cutting height, the collapse of the overlying strata gradually reached a symmetric distribution with increasing height. The deformation of the retained roadway was mainly concentrated on the roof, and the maximum deformation was 14 mm near the roof cutting side. A numerical simulation of the original size of the model test proved that the laws of strata movement and surrounding rock deformation were consistent with the physical test results. Finally, field measurements were performed, which verified the rationality of this study.

**Keywords:** gob-side entry retaining by roof cutting; model test; non-contact monitoring system; strata movement; numerical simulation; mine pressure monitoring

## 1. Introduction

Due to high construction cost, gas accumulation, and excessive deformation of the surrounding rock when using traditional gob-side entry retaining (GSER) with backfill, a new roof cutting type GSER has been developed [1–4]. Having been applied to more than 500 coal mines in China, this new method became popular and achieved great economic benefits. At present, most research on this technology is focused on field application, while there are few theoretical studies on the changing law of overlying strata movement and the deformation of the retained roadway [5–7]. Therefore, this study mainly uses model testing and numerical analysis to better develop a fundamental understanding of this technique and address the gap in basic theoretical research.

The new GSER method is performed by roof cutting to make the rock strata over the goaf collapse smoothly and form a roadway rib, replacing the traditional filling body [8–10]. The construction technology necessary for this method is currently maturing. Gao et al. [11], Wang et al. [12], and Guo et al. [13] performed a field application of this “110 mining method” on thick, medium-thick, and thin coal seams, respectively, and achieved good results. The technology has been developed in the recent years; hence, no systematic study has yet been performed on basic theories such as the changing movement law of the overlying strata and the deformation law of the retained roadway

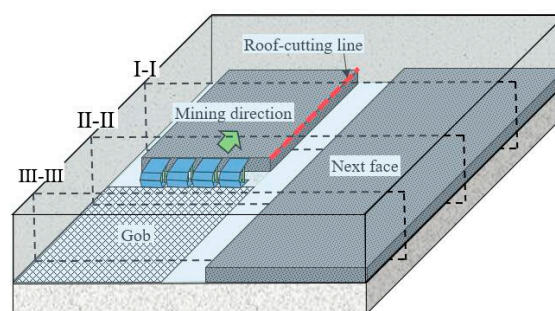
surrounding rock [14]. Currently, the movement and deformation laws are mainly studied through an indoor model test. The main advantage of carrying out the model test is that through a reasonable similar design, it can qualitatively analyze the large-scale overlying rock movement of the stope, which cannot be accomplished by field research [15,16]. Meanwhile, its main disadvantage is that the traditional monitoring means in the test is relatively outdated. The commonly used total station monitoring system can measure less monitoring points with a large error, which is basically at a cm level; hence, the deformation law of the roadway and the strata movement are difficult to accurately reflect. Therefore, this study introduces a non-contact full-field deformation monitoring system, called the “high-precision digital speckle imaging system”, and applies it to the model test [17,18]. This monitoring system has been applied in small-scale material engineering because of its high data collection sensitivity, small error, and high precision. On the contrary, the large-scale three-dimensional geological model test is not widely used.

This study will focus on the changing law of the overburden strata movement, deformation law of retained roadways, and distribution law of the surrounding rock stress under the conditions of the roof cutting type GSER. First, a simplified mechanical model is established and roof deformation is deduced according to the structural characteristics of the surrounding rock. Second, based on the similarity theorem, the physical model test based on the field prototype is designed and performed; the non-contact full-field deformation monitoring system is used for monitoring in the test; and a numerical model with the same size as that in the test is established for a comparative analysis. Finally, the test and simulation results are verified by field monitoring. The results of this study provide theoretical guidance for the field application of this important new method.

## 2. Gob-Side Entry Retaining by Roof Cutting

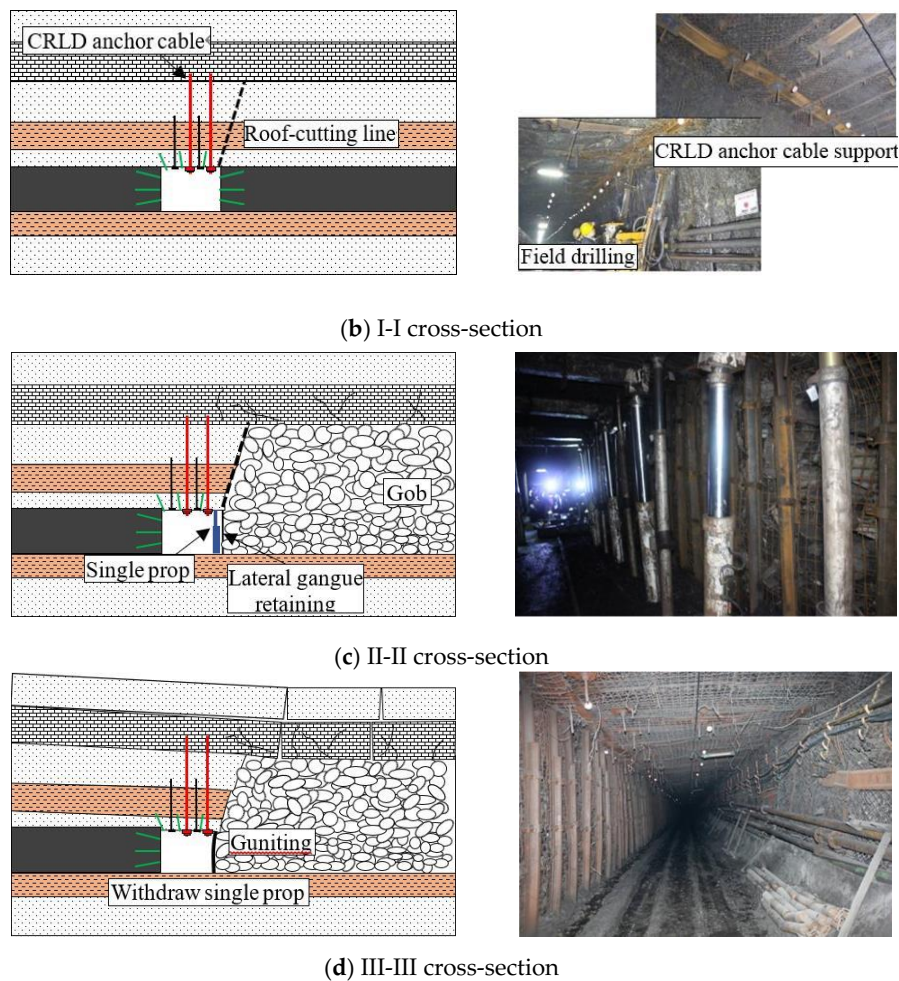
### 2.1. Technological Process

Figure 1 shows GSER by roof cutting, installation of the CRLD anchor cable plus roof cutting, temporary gangue retaining support, and withdraw temporary support [5,8]. It consists of four general steps. The first step is to install the constant resistance and large deformation (CRLD) anchor cable on the pre-reserved roadway roof to reinforce the original support system. The second step is roof-cutting at a certain distance ahead of the working face, as shown in Figure 1b. The third step is to build gangue retaining support along the roof cutting line after the mining, so that the caved rock in goaf can form the roadway rib, as shown in Figure 1c. The fourth step is to withdraw the temporary support (e.g., single pillars) after the roadway remains stable, before grouting to isolate the goaf, which is conducive to air circulation, shown in Figure 1d.



(a)

Figure 1. Cont.



**Figure 1.** (a) GSER by roof cutting, (b) Installation of CRLD anchor cable + Roof cutting, (c) Temporary gangue retaining support, (d) Withdraw temporary support.

2.2. Principle

Figure 2a shows the traditional structure of GSER [19]. When the working face is mined, the overlying strata regularly break, and block B rotates and subsides, entering the “given deformation” state, which compresses the filling body and the solid coal, and causing deformation and failure of the surrounding rock [20,21]. At the same time, the load is transferred to the surrounding rock of the retained roadway because of the mutual extrusion of key blocks A, B, and C in the articulated beam structure, resulting in an increased stress concentration degree and an aggravated deformation. Figure 2b depicts the structure of the roof cutting type GSER. First, it cuts off the articulated beam structure formed by the mutual extrusion of the key strata above the retained roadway, that is, it eliminates the stress transfer path and reduces the stress concentration degree. Second, by utilizing the bulk increase character of the rock mass, the caved rock fills the goaf, which has a certain supporting force on the upper strata, and significantly reduces the rotational subsidence of the broken rock blocks. This reduces the compression damage to the surrounding rock on the retained roadway. Through roof cutting, a wedge-shaped confined zone is formed above the entry, which is beneficial to the stability of the retained roadway.

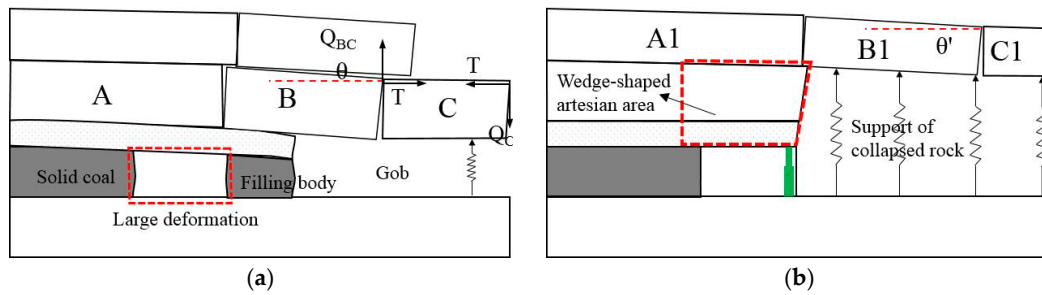


Figure 2. Schematic diagram (a) Traditional GSER, (b) The GSER by roof cutting.

2.3. Mechanical Model

Simplify the wedge-shaped confined zone in Figure 2b to obtain the mechanical model shown in Figure 3a. It can be known that the model is a cantilever beam structure with a fixed end on the left and a free end on the right. The length is  $l$  and the height is  $b$ . The upper surface is subjected to uniform pressure from overlying strata, and the load collection degree is  $Q_1$ . Considering the effect of support in the roadway, the force on the lower surface is simplified to mean force, and the average load collection degree is  $Q_2$ . The right end of the cantilever beam is supported by a single pillar, i.e., the right end is supported by a concentrated force,  $F = fa$ . The right-side obliquity is supported by caved rock, which is simplified to a uniform force, and the load concentration is  $q$ . As shown in Figure 3b, the cantilever beam structure is divided into rectangular and triangular parts. Because the deformation of the two parts is the same, only rectangular displacements are solved.

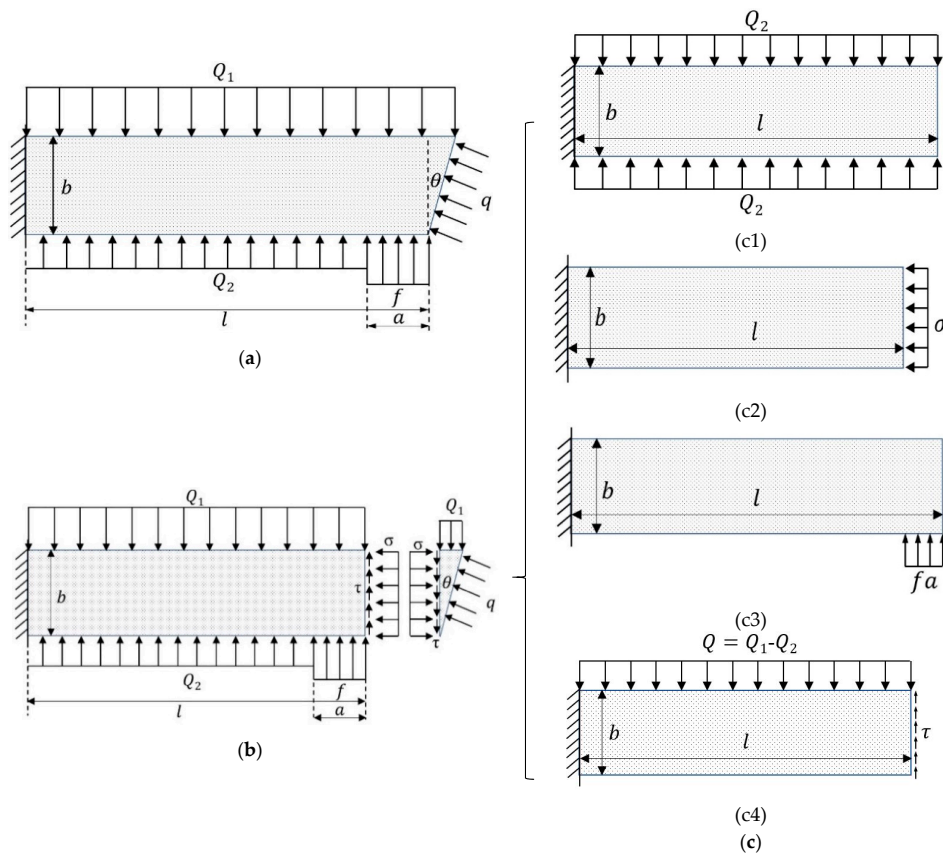


Figure 3. Cantilever beam model. (a) Full force model, (b) Model decomposition, (c) Decomposition of rectangular roof model, (c1) Bilateral compression model, (c2) Unilateral compression model, (c3) Concentrated force model, (c4) Upper uniform pressure model.

According to the superposition principle of material mechanics [22], the force on a rectangular cantilever is decomposed into four parts as shown in Figure 3c, and their deflections are solved, respectively. The final solution of the mechanical model, as shown in Figure 3a is obtained by superimposing each result.

After solving the mechanical model in Figure 3c, the results showed that the upper and lower boundaries of Figure 3c1 were subjected to a uniform pressure, while the right boundary of Figure 3c2 was subjected to a uniform lateral pressure. Both these results can be regarded as uniaxial compression. The cantilever has no deflection under these two boundary conditions, that is:

$$W_1 = W_2 = 0 \tag{1}$$

For the mechanical model shown in Figure 3c3, where the right end was subjected to a concentrated force,  $F = fa$ , the deflection can be obtained as follows:

$$M_3 = Fl - Fx \tag{2}$$

$$\frac{d^2w}{dx^2} = \frac{Fl - Fx}{EI} \tag{3}$$

$$W_3 = \frac{1}{EI} \left( \frac{1}{2}Flx^2 - \frac{1}{6}Fx^3 \right) + Cx + D \tag{4}$$

From  $\theta(0) = 0$  and  $W(0) = 0$ , it follows that  $C = 0$  and  $D = 0$ . Therefore, the deflection under this condition is

$$W_3 = -\frac{Fx^2}{6EI}(3l - x) \tag{5}$$

For the mechanical model shown in Figure 3c4, the model was further decomposed, as shown in Figure 4a,b. According to Saint Venant's principle, the right end shear stress  $\tau$  in Figure 4a can be simplified to a concentrated force  $K = \tau b$ , and the deflection can be obtained as follows:

$$W_{4-1} = -\frac{Kx^2}{6EI}(3l - x) \tag{6}$$

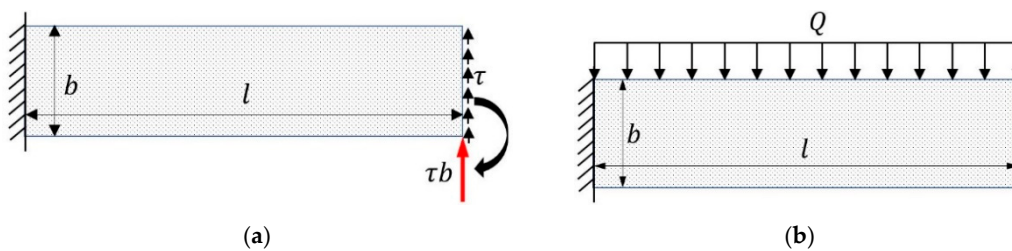


Figure 4. Mechanical model decomposition. (a) Shear force model, (b) Uniform pressure model.

For Figure 4b:

$$M_4 = \frac{1}{2}Ql^2 - Qlx + \frac{1}{2}Qx^2 \tag{7}$$

$$\frac{d^2w}{dx^2} = \frac{1}{EI} \left( \frac{1}{2}Ql^2 - Qlx + \frac{1}{2}Qx^2 \right) \tag{8}$$

From  $\theta(0) = 0$  and  $W(0) = 0$ , it follows that  $C = 0$  and  $D = 0$ . Therefore, the deflection under this condition is

$$W_{4-2} = \frac{Qx^2}{6EI}(x^2 - 4lx + 6l^2) \tag{9}$$

From these results, the overall cantilever beam deflection is obtained as follows:

$$\begin{aligned}
 W &= W_1 + W_2 + W_3 + W_{4-1} + W_{4-2} \\
 &= \left[ \frac{Qx^2}{6EI} (x^2 - 4lx + 6l^2) \right] - \left[ \frac{Kx^2}{6EI} (3l - x) \right] - \left[ \frac{Fx^2}{6EI} (3l - x) \right] \\
 &= \frac{x^2}{6EI} \{ Q(x^2 - 4lx + 6l^2) - (k + F)(3l - x) \}
 \end{aligned}
 \tag{10}$$

By simplifying the actual structure on the site, we establish a corresponding mechanical model and show that the deflection deformation on the right end of the cantilever is the largest. In other words, the deformation is largest on the roof cutting side, and corresponding supporting measures should be implemented there to ensure the stability of the retained roadway.

### 3. Project Overview

#### Geological Conditions

The 200 working face of Dianping Coal Mine is selected as the prototype of simulation experiment. Figure 5a shows the location of the mine. Figure 5b shows the layout of the working face. The average buried depth is 600 m, the length along the tendency is 220 m, and the strike length is 1080 m. The length of designed retained roadway is 1088 m, which is the test section marked by the red dashed line. The dip angle of the working face is 2–8°, average 4°. Figure 5c shows the roof and floor strata histogram. The thickness of the coal seam is 3.1 m. The entry section is rectangular, 3 m high and 5 m wide. The direct floor is sandy mudstone with a thickness of 3.3 m. The hard floor is fine sandstone with a thickness of 2.8 m. From bottom to top, there are 2.1 m thick sandy mudstone, 6.1 m thick medium-sized sandstone, 0.7 m thick sandy mudstone, 2.4 m thick coal interlayer, and 6.0 m thick limestone. In addition, the in-situ stress test shows that there is no obvious horizontal tectonic stress in stope, and the vertical stress is the main stress. Figure 5d shows the roof-cutting support parameters.

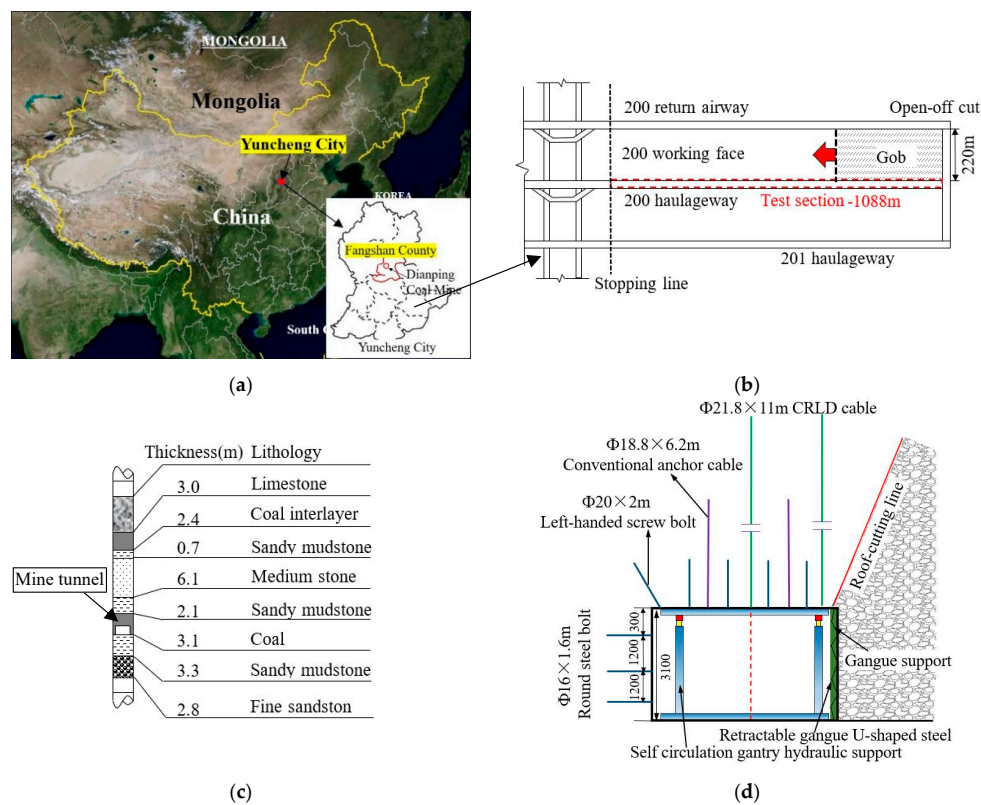


Figure 5. (a) Geographical overview (b), Working face layout, (c) Roof and floor lithology, (d) Support section.

## 4. Model Experiment

### 4.1. Testing System

Figure 6 depicts the experimental system used in this study. The test system consists of console and main engine structure. The size of the test machine is length  $\times$  width  $\times$  height: 3310 mm  $\times$  970 mm  $\times$  3010 mm, the maximum accommodation physical model size is 1600 mm  $\times$  400 mm  $\times$  1600 mm. The inner boundary of the model is the hydraulic pressure head which can be controlled independently. The loading range is 0–15 MPa, and the minimum loading accuracy is 0.1 MPa, it also can maintain constant pressure for long-term model tests.

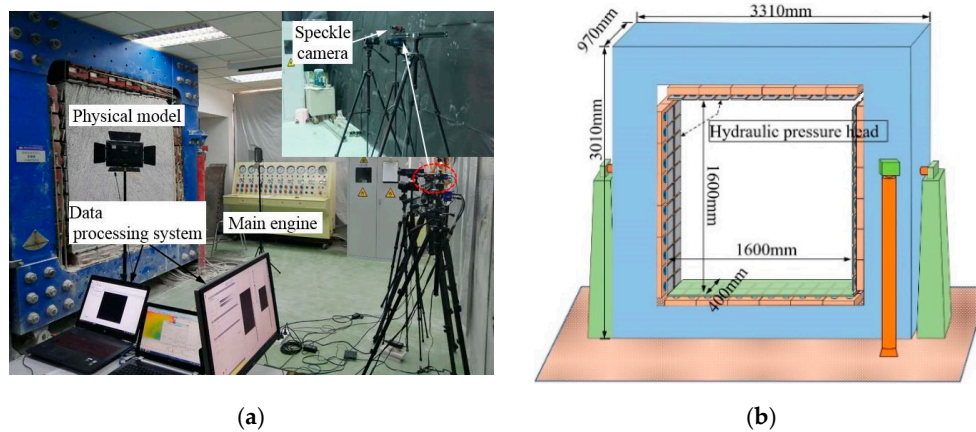


Figure 6. Experimental System. (a) Field layout of experimental tools, (b) Structure of model testing machine.

### 4.2. Test Monitoring System

Figure 7 shows the basic structure and calculation principle of the high-precision digital speckle imaging system primarily used for the analysis of the model surface strain and displacement. The system was composed of a data acquisition system (AVT industrial camera), a data analysis system, etc. The speckle camera resolution in Figure 6 was 5 million px. The precision of the displacement pixels measured by the system was 0.001–0.01 cm. The strain precision was 20–50  $\mu\epsilon$ . The strain range was 0.01–2000%.

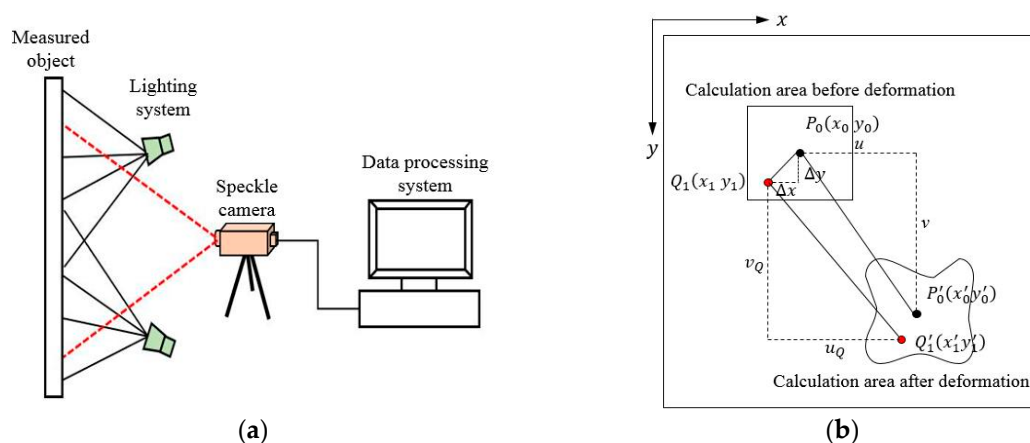


Figure 7. (a) Monitoring system and (b) calculation principle.

Figure 7b illustrates the system’s working principle. Suppose that  $P_0(x_0, y_0)$ ,  $P'_0(x'_0, y'_0)$  is the coordinate of the center point of the sub-area before and after the deformation.  $Q_1(x_1, y_1)$ ,  $Q'_1(x'_1, y'_1)$

is the coordinate of any point in the calculation sub-area, which can be seen from the deformation of the figure [17,18]:

For  $P_0, P'_0$ :

$$\begin{cases} x'_0 = u + x_0 \\ y'_0 = v + y_0 \end{cases} \quad (11)$$

For  $Q_1, Q'_1$ :

$$\begin{cases} x'_1 = u_Q + x_1 \\ y'_1 = v_Q + y_1 \end{cases} \quad (12)$$

The figure shows that  $\Delta x$  and  $\Delta y$  are the distances from point  $Q_1$  to point  $P_0$  in the X and Y directions, respectively:

$$\begin{cases} x'_0 = \Delta x + x_0 \\ y'_0 = \Delta y + y_0 \end{cases} \quad (13)$$

At the same time, the object will produce rotation, stretching, compression, shear, and other single or combinations of failure because of its rigid body displacement. Therefore, according to the theory of continuum mechanics,  $u_Q$  and  $v_Q$  can be approximately expressed by displacement and its first derivative, respectively.

$$\begin{cases} u_Q = u + \frac{\partial u}{\partial x} \Delta x + \frac{\partial u}{\partial y} \Delta y \\ v_Q = v + \frac{\partial v}{\partial x} \Delta x + \frac{\partial v}{\partial y} \Delta y \end{cases} \quad (14)$$

In combination with (11)–(14):

$$\begin{cases} x'_0 = x_0 + u + \frac{\partial u}{\partial x} \Delta x + \frac{\partial u}{\partial y} \Delta y \\ y'_0 = y_0 + v + \frac{\partial v}{\partial x} \Delta x + \frac{\partial v}{\partial y} \Delta y \end{cases} \quad (15)$$

where  $u$  and  $v$   $\frac{\partial u}{\partial x}$ ,  $\frac{\partial u}{\partial y}$ ,  $\frac{\partial v}{\partial x}$ ,  $\frac{\partial v}{\partial y}$  represent the displacement and the derivative of the midpoint in the subdomain, respectively.

The similar proportion of the geological model test is usually large; the error of the traditional measurement method is basically in the centimeter range, and the selected monitoring points are limited. Therefore, the error is also large. The model displacement monitoring error can be controlled within 0.001–0.01 cm using the high-precision digital speckle imaging system, thereby greatly reducing the measurement error in the test process and making the analysis results more convincing.

### 4.3. Model Test

#### 4.3.1. Model Similar Design

Figure 8 shows the model design. Table 1 presents the similarity parameters. Due to the limited space in test-bed (maximum model size 1600 mm × 400 mm × 1600 mm), the size of the retained roadway in test must be determined first. The size of retained roadway used in this study is length × height: 100 mm × 60 mm. Because the actual size of the retained roadway is length × height: 5 m × 3 m, we conclude that the geometric similarity ratio is  $C_L = L_P/L_M = 50$ . (Subscript  $P$  represents the parameters of the prototype, Subscript  $M$  represents the parameters of the experimental model.) The volume-weight ratio  $C_\rho \approx 1$  can be measured by laboratory mechanical experiments, resulting in a stress similarity ratio of  $C_\sigma = C_L \cdot C_\rho = 50$  and a deformation modulus similarity ratio of  $C_E = C_\sigma \cdot C_\varepsilon = 50$ . The similar ratio of strain, internal friction angle, friction coefficient, and Poisson's ratio is equal to 1. As shown in Figure 8, the physical model is determined according to the similarity ratio, including the thickness of each stratum and boundary condition.

Table 1. Similarity parameter.

Geometric similarity ratio	$C_L = 15$
Volume-weight ratio	$C_\rho \approx 1$
Stress similarity ratio	$C_\sigma = 15$
Deformation modulus similarity ratio	$C_E = 15$
Similar ratio of strain, friction angle, friction coefficient, Poisson's ratio	$C_\epsilon = C_\alpha = C_f = C_\mu = 1$

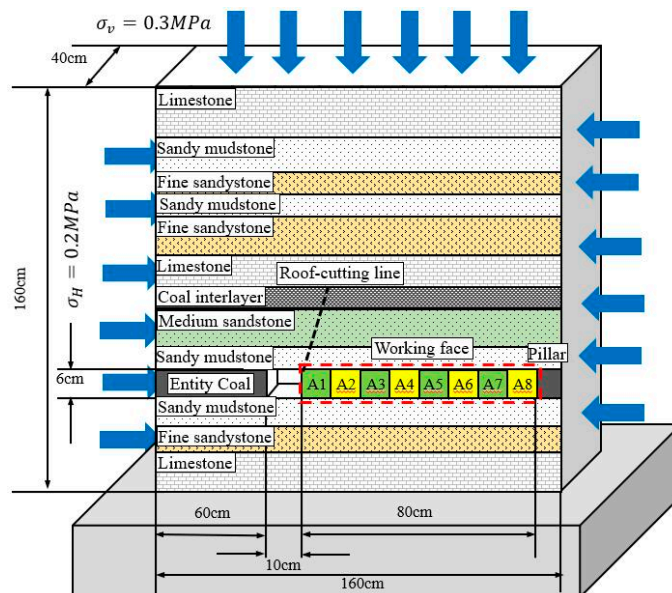


Figure 8. Model design.

The following five kinds of rock strata materials with different strengths and deformation characteristics were prepared for this model test: coal rock, sandy mudstone, fine sandstone, medium sandstone, and limestone. These rock materials are mainly composed of fine river sand, barite powder, gypsum, talc powder, mica powder, and water at different mixing ratios [19,23]. For each proportionally mixed material, a cylindrical standard rock sample with 50 mm diameter and 100 mm height was prepared according to the laboratory rock mechanics experiment standards and tested through the infinite lateral compression and Brazilian splitting tests [24]. The final ratio was determined when the strength value was consistent with the theoretical calculation result. Figure 9 shows relevant pictures of the indoor mechanics experiment. Table 2 presents the physical and mechanical parameters of each rock material.



Figure 9. The mechanical test.

Table 2. Mechanical parameters.

No.	Lithology		UCS (MPa)	Tensile Strength (MPa)	Elastic Modulus (GPa)	Cohesion (MPa)	Internal Friction angle (°)	Unit Weight (kN/m <sup>3</sup> )
1	Limestone	Prototype	85	5.21	3.73	11	41	2730
		Model	1.7	0.104	0.075	0.22	41	2730
2	Sandy mudstone	Prototype	16	0.6	1.2	1.5	36	2630
		Model	0.32	0.012	0.024	0.03	36	2630
3	Fine stone	Prototype	32	1.19	1.1	2.2	35	2500
		Model	0.64	0.024	0.022	0.044	35	2500
4	Coal	Prototype	14.5	0.35	1.5	0.86	20	1400
		Model	0.29	0.007	0.03	0.0172	20	1400
5	Medium sandstone	Prototype	63	4.13	2.2	6.3	40	2600
		Model	1.26	0.083	0.044	0.126	40	2600

### 4.3.2. Excavation Design

Figure 10 shows the excavation plane. The whole excavation was divided into six stages [25]. The first stage is the roadway excavation, where the roadway support was neglected. Second is the working face excavation. The strike length of the working face was 40 cm. The excavation was divided into five groups. The first group of “coal seam” can be normally excavated. On the contrary, excavating the remaining groups was difficult because of the collapse of the overlying strata. Therefore, steel brackets were designed to replace the coal seam, and the coal seam excavation was simulated by extracting the designed length behind the model. The excavation length along the strike of each group was 8 cm, and the simulated site excavation was 4 m. Each group was further divided into eight groups along the tendency. The excavation direction of each group was from 1 to 8. After the excavation completion in each step, it will remain stationary for no less than 20 min until the strata movement stabilizes.

The roof cutting in our test was pre-reserved in the process of laying the model because of the limitation of the laboratory test conditions. The damage of the surrounding rock mass caused by roof cutting was simulated by manually inducing random and varying degrees of damage on both sides of the cutting seam during the reservation process.

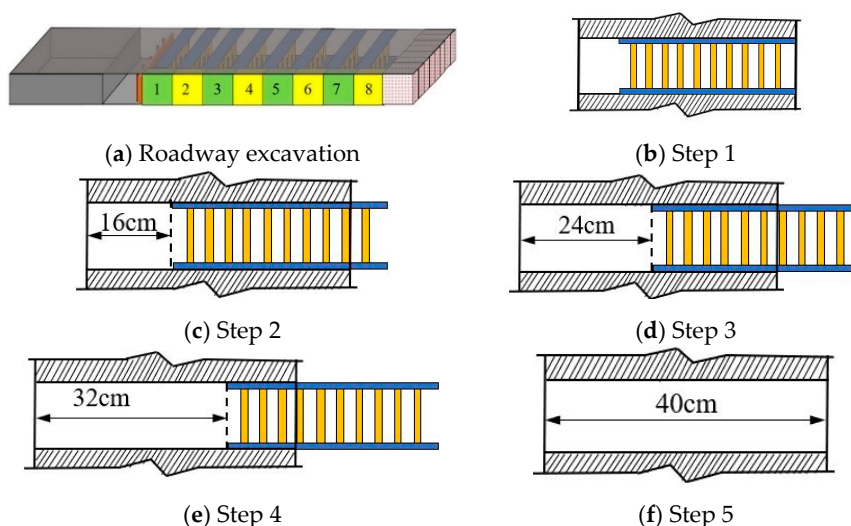


Figure 10. Excavation Scheme. (a) Roadway excavation, (b) Excavation 8cm, (c) Excavation 16cm, (d) Excavation 24cm, (e) Excavation 32cm, (f) Excavation 40cm.

### 4.3.3. Monitoring Design

The experiment primarily monitored the model surface displacement field and the deformation characteristics of the retained roadway. A high-precision digital speckle imaging analysis system was used to analyze the displacement characteristics [25]. A TV3000 static strain indicator was used to monitor the strain variation law of the surrounding rock and the solid coal. An infrared thermal imager was utilized to monitor the variation of the temperature field of the model. Figure 11 illustrates the monitoring line of each rock stratum, which was 1 cm away from the bottom of the rock stratum. The figure also presents the layout of the deformation monitoring points on the retained roadway.

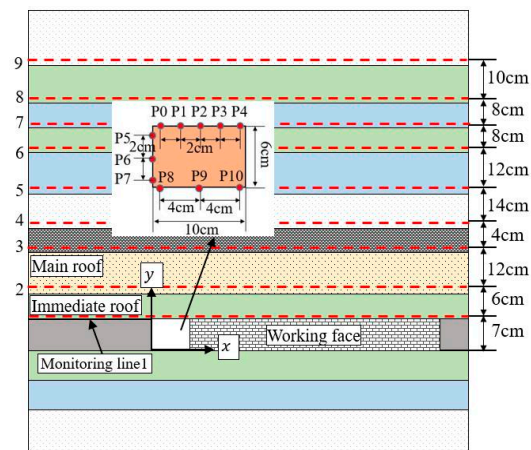


Figure 11. Monitoring scheme layout.

## 4.4. Results

### 4.4.1. Experimental Process

According to the experimental results, the movement of the overlying strata can be divided into three main stages. Figure 12a,b depict the first stage, where the immediate roof had an obvious bending subsidence, and an abscission layer was generated. The immediate roof (Figure 12b) completely collapsed when the working face was excavated for 12 m. Affected by the roof cutting, the roof stratum along the cutting seam broke, and the collapse was relatively complete. The filling height of Area A was higher than that of the other goaf locations because of the expanding characteristics of the broken rocks. The collapse of the rock strata on the uncut side formed a triangle area. The collapse degree was incomplete compared to that on the cut side.

Figure 12c,d show the model state when the working face was excavated for 16 m. In this stage, the immediate roof was compacted; the main roof on the left side fell regularly as a whole; and an open fracture zone was formed on the right side, where the fissures were relatively well developed. The coal interlayer above the main roof and its upper strata clearly subsided.

Figure 13 shows the third and final stage, in which the overlying strata movement reached a stable state. The rock strata on the roof cutting side collapsed along the cutting seam, filling the space below. Under the influence of coal mining, the movement of the rock strata developed upward to the hard and thick limestone rock layer, *f*, which was 58 cm away from the coal seam. The rock caving area can be roughly divided into three parts, namely the well-filled zone on the roof cutting side, the compaction zone in the middle and left sides, and the fracture developed zone on the uncut side. Overall, the fracture line of the rock strata on both sides of the stope developed into an asymmetric curve. The wedge-shaped compression area formed by the roof cutting above the retained roadway showed an obvious bending deformation, and the roof subsidence on the roof cutting side was the largest. A distinct main crack was observed in the fine sand stratum 43 cm above the goaf. According to

the test field measurement, the affected area of the overburdened strata movement caused by mining was 58 cm, which is approximately 9.67 times of the mining height.

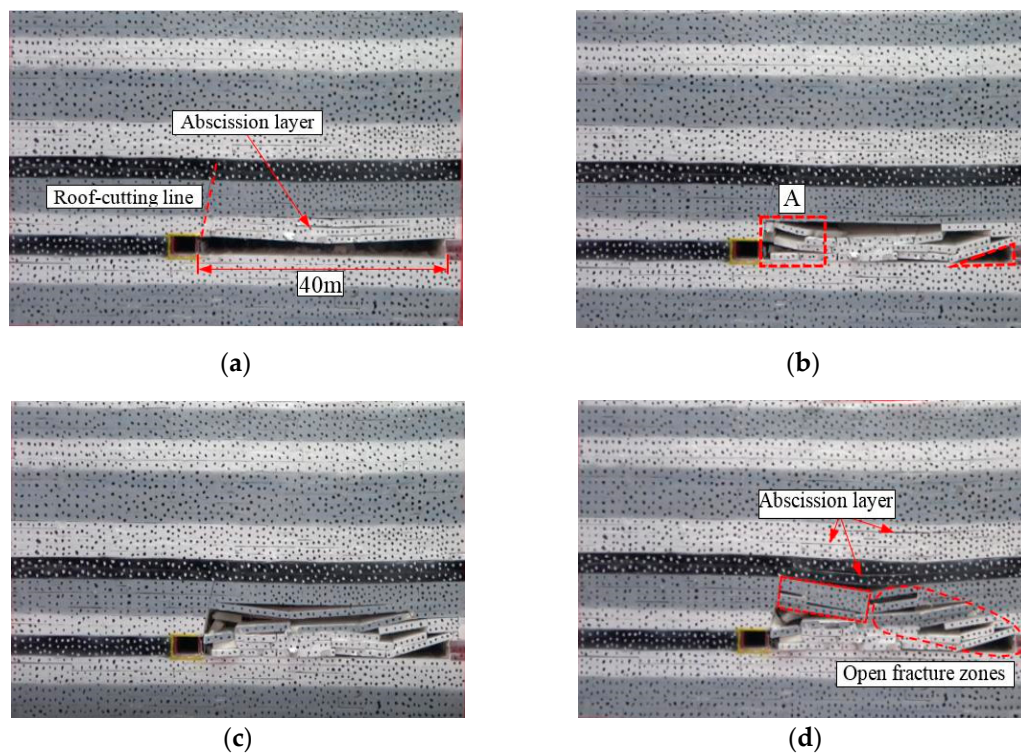


Figure 12. (a,b) The first stage: the collapse of direct roof. (c,d) second stage: collapse of main roof.

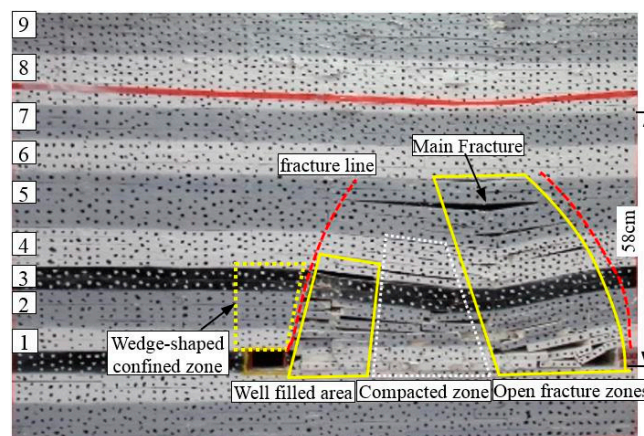
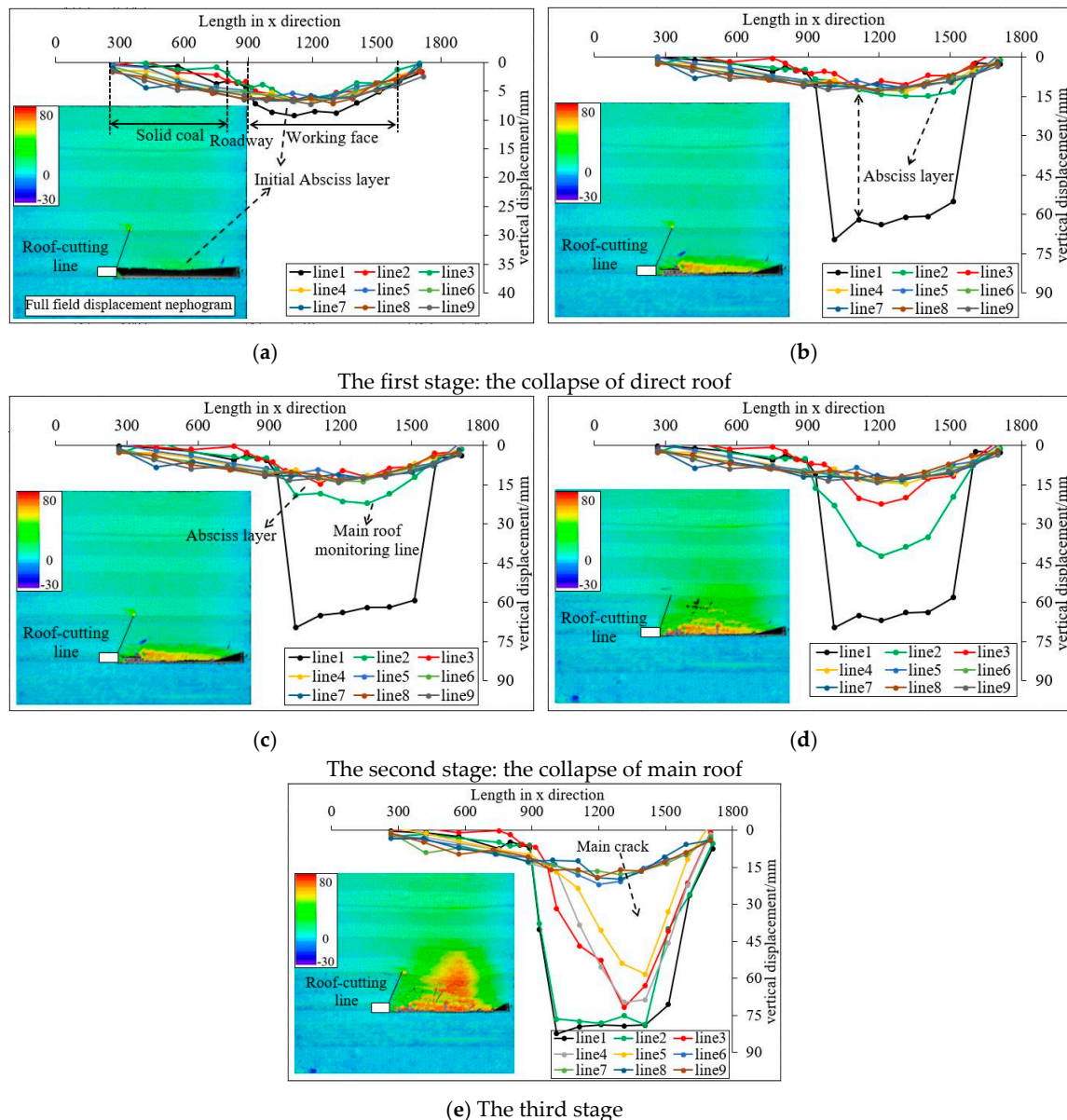


Figure 13. The third stage.

#### 4.4.2. Displacement Analysis

Figure 14 shows the displacement curve of each rock stratum monitoring line and the full-field displacement cloud map of the model. As shown in Figure 14a,b, in the first stage, direct roof monitoring line 1 had larger bending and subsidence compared to the other rock monitoring lines, with a maximum of 12 mm located in the center left. Some small abscission layers can also be found in the direct roof strata. The monitoring line subsidence was bounded by the roof cutting line until the direct roof completely collapsed. The displacement of the solid coal side and the retained roadway roof remain unchanged, while the displacement in the goaf was relatively large. The displacement of the overall cutting side was larger than that of the uncut side.

Figure 14c,d illustrate the displacement curve corresponding to the second stage, which is the collapse of the main roof. Under the support of the collapsed direct roof, the maximum subsidence of the main roof was 46 mm. Influenced by the roof cutting, the displacement of the main roof near the cutting seam was large, and the direct and main roof subsidence presented an asymmetric distribution feature.



**Figure 14.** Strata displacement curve. (a) Excavation 8cm, (b) Excavation 16cm, (c) Excavation 24cm, (d) Excavation 32cm, (e) Excavation 40cm.

Figure 14e shows the displacement curve corresponding to the stable stage of the rock stratum movement. An obvious displacement difference was obtained between monitoring lines 5 and 6. That is, an abscission layer existed between the rock layers, where Monitoring line 6 was located, was a 5m-thick hard limestone rock layer, which produced bending, but not fissure, under the action of gravity from the overburdened rock. The displacement of the cut side was larger than that of the uncut side within the height of the roof cutting. The average displacement of the wedge-shaped confined zone formed by the roof cutting above the retained roadway was less than 15 mm, thereby yielding a relatively stable entry roof. It also known that the maximum subsidence of monitoring line 1 is about

75 mm, which is greater than the thickness of coal seam 60 mm. This is because there is a stress loading process before the excavation of the working face, and the gap between the materials in the process of laying the model cannot be avoided artificially. However, with the increase of the stress, the gap is gradually compacted, resulting in a compressive deformation of the model as a whole.

According to the abovementioned analysis, in the early stage of the rock strata movement, the rock mass near the cutting seam collapsed first because of the roof cutting, thereby creating a displacement larger than that on the uncut side. The displacement within the cutting height is characterized by an asymmetric distribution. In the later stages, better filling effects on the roof cutting side caused the bending subsidence value of the upper rock mass to be smaller than that of the uncut side. In other words, the roof cutting only affects the collapse law of the rock strata in a certain range near the cutting site.

#### 4.4.3. Analysis of the Retained Roadway Deformation

Figure 15a shows the displacement curve of the roof measurement points. The subsidence of the P4 point was the largest with a maximum value of 14 mm. The subsidence decreased at points farther away from the roof cutting seam. Figure 15b depicts the horizontal displacement curve of the measuring points on the solid coal. The horizontal displacement of measuring point P6 in the middle obtained a maximum value of 7 mm. Shown in Figure 15c, the displacement of the measuring points at the bottom was the smallest. The maximum vertical displacement of the floor was 4 mm with a slight floor heave.

Figure 15d exhibits the roadway deformation diagram drawn by the monitored displacement value. The roof deformation is clearly seen. The subsidence was the largest on the roof cutting side. The deformation of the solid coal and floor was relatively small. We conclude from this data analysis that the effect of retaining the roadway in the mining process was improved using this method.

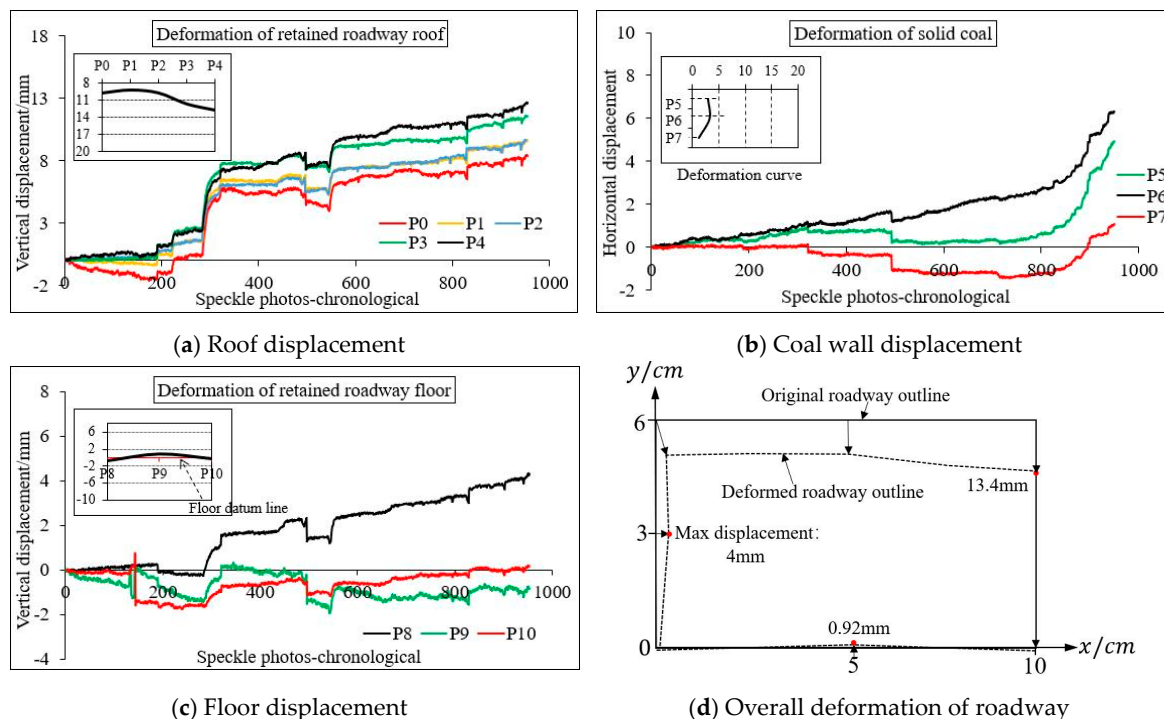


Figure 15. Displacement curve of retained roadway surrounding rock.

### 5. FLAC3D Modeling

#### 5.1. Model Setup and Calibrations

The movement law of the overlying strata and the deformation law of the retained roadway surrounding rock can be quantitatively analyzed using the physical model test date. We verified the rationality of the rules summarized in the model test by using FLAC3D numerical simulation software (V5.0, Itasca Consulting Group, Inc, Minneapolis, MN, USA) to assist the research. This software is mainly used to simulate and calculate the mechanical behavior of rock and soil materials and the plastic flow of rock and soil materials after reaching the yield limit, which is better for a large deformation. Accordingly, we established a numerical model of the same scale as the physical model through FLAC3D simulation software [26,27]. This also allowed further study of the model’s stress evolution law of the surrounding rock of the stope and the retained roadway after the roof cutting.

On the basis of the original size of the physical model, the numerical model shown in Figure 16a expanded to 0.5 m and 1.6 m along the x and y directions, respectively, thereby resulting in a model size of 2.2 m (length) × 2 m (width) × 1.6 m (height) while the actual simulation size was 110 m × 100 m × 80 m. The grid was refined near the coal seam and the roadway. The displacement boundary constraint was adopted. The velocity of the left and right boundaries of the model was zero in the x direction; that of the front and rear boundaries was zero in the y direction; and that of the bottom boundary was zero in the x, y, and z directions. The upper boundary was a free boundary, and the self-weight load of the overlying strata was 0.2 MPa. The physical, mechanical, and geometric parameters of the rock mass were determined based on the field’s original rock parameters. The Mohr Coulomb model was used as the constitutive model of the rock mass. The empty element model was used to simulate roadway driving and working face mining. Figure 16b,c show the model boundary conditions and the working face layout. Table 2 presents the physical and mechanical parameters of each rock layer.

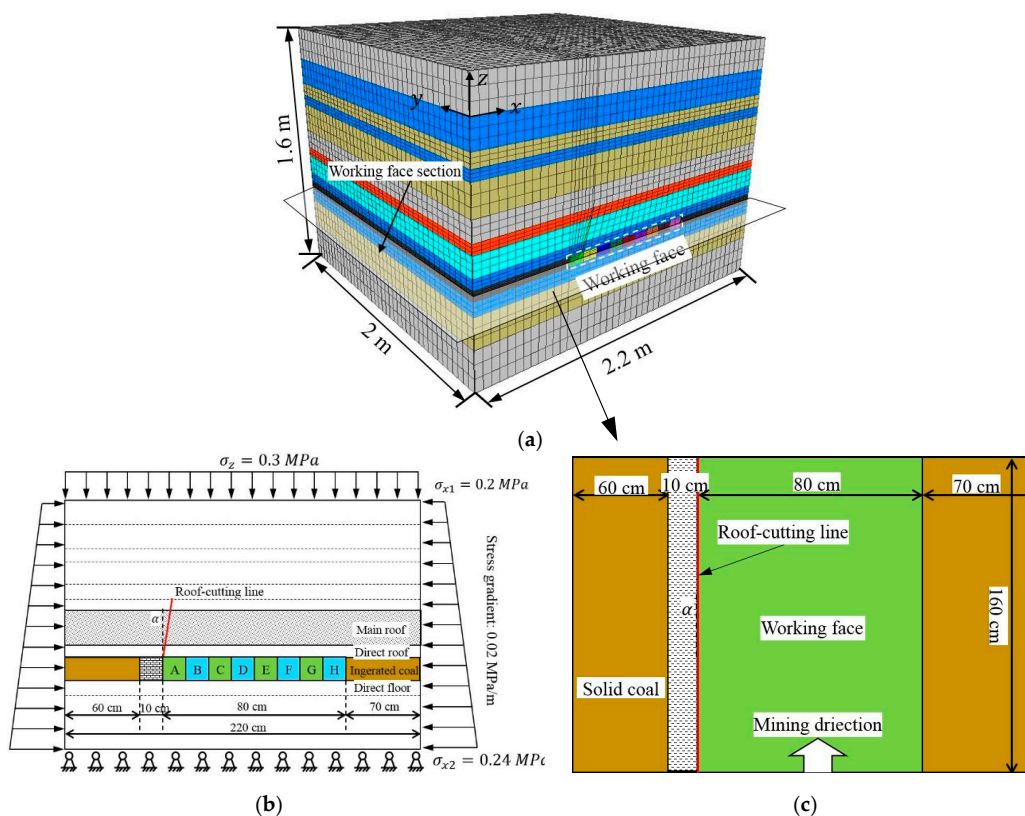
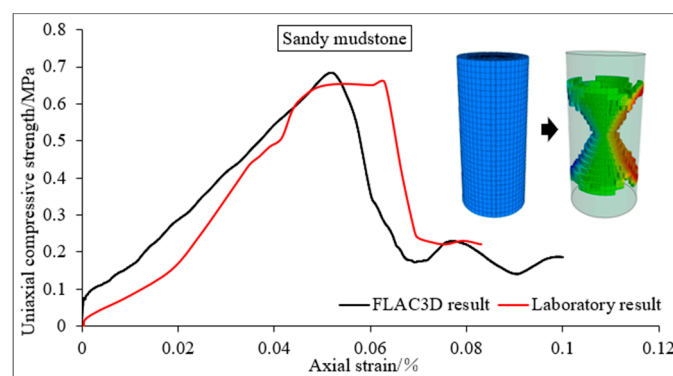


Figure 16. (a) Numerical model (b) boundary condition and (c) layout of the working face.

We used sandy mudstone as an example and established a model specimen with 50 mm diameter and 100 mm height for the numerical simulation of the uniaxial compression to ensure that the mechanical parameters of each lithology were reasonable. We simulated the stress loading of actual indoor mechanical tests by constraining the top and bottom surfaces and applying a certain displacement velocity. Figure 17 shows the stress–strain curves of the rock specimen under the numerical simulation and laboratory experiment conditions. The numerical simulation results indicated that the specimen exhibited an “x-type shear failure” similar to the indoor test. As shown in the stress–strain curve, the peak value of the compressive strength in the laboratory experiment was slightly lower than the simulation value, while the specimen failure lagged behind the simulated compression curve because the actual rock specimen still had a certain residual strength after failure. The results showed that the numerical calculations corresponded well to the experimental results. In other words, the mechanical parameters were reasonable.



**Figure 17.** Comparison of the stress–strain curve between the numerical model and laboratory test.

## 5.2. Simulation Results

### 5.2.1. Analysis of the Strata Movement

The monitoring lines in the numerical simulations were consistent with those in the model test. Figure 18a,b show the comparison diagrams of the subsidence displacement curve between the numerical simulation and the laboratory tests. The solid line in the figure depicts the numerical simulation result, while the dotted line represents the model test result. Figure 18a corresponds to the main roof collapse stage in the model test. The coal seam at this stage was excavated for 12 cm, i.e., to simulate the actual excavation of 6 m. The vertical displacement of the roadway roof beside the roof cutting line was small, and the maximum displacement of the immediate roof subsidence was 55 mm; as a result of the parameter verification, it can be concluded that the actual subsidence is 3.3 m through the geometric similarity ratio, which is consistent with the actual situation, indicating that the strata on the roof cutting side caved fully. The subsidence curve was asymmetrical, and the deformation on the roof cutting side was larger than that on the uncut side. The maximum subsidence value of the main roof was 27 mm, which is 1.35 m in actual situation, it shows that due to the full collapse of the direct roof strata on the roof cutting side, it has a certain supporting effect on the upper basic roof and reduces the subsidence. The subsidence curve was also asymmetrical. Monitoring lines 5 and 6 showed that the upper strata were less affected by the coal seam excavation, expressing small deformation values. The displacement trend of the direct roof monitoring line was nearly identical to that observed in the laboratory test, although the latter had a higher measured value than the simulation. This result is attributed to the model having additional compression deformation accompanied by stress loading in the laboratory test, while the simulation was able to monitor only the subsidence displacement caused by the excavation.

Figure 18b corresponds to the model test stable stage of the rock stratum movement. As shown in the displacement nephogram, within the height of the roof cutting, the displacement of the rock

strata decreased as the distance from the roof cutting line increased, indicating that the roof cutting side strata more fully collapsed. Less effect was observed outside of the roof cutting height, and the subsidence curve showed a symmetrical distribution. The overall subsidence trends of the test and simulation curves were identical.

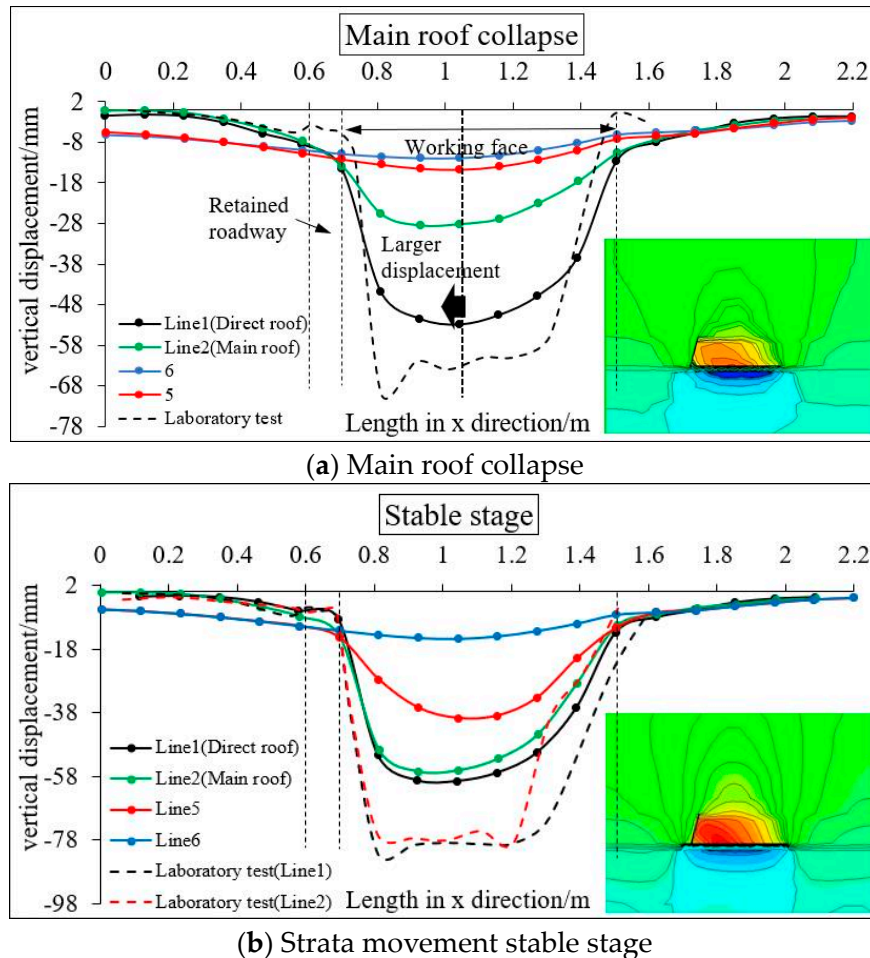


Figure 18. Displacement comparison analysis.

### 5.2.2. Analysis of the Stress Distribution Law

Figure 19a shows the full-field vertical stress diagram when the working face was excavated for 1.0 m. Figure 19b presents the monitoring line layout. Figure 19c,d show the stress distribution on monitoring line. Figure 19c illustrates that varying degrees of stress concentration existed on both sides of the stope. Moreover, the stress concentration along the solid coal seam was not obvious, and the maximum concentration stress value on the roof cutting side was approximately 0.25 MPa. The stress concentration on the uncut side was higher with a maximum value of approximately 0.29 MPa compared with the uncut side. The stress value decreased by 16%. Figure 19d shows the advance stress of the working face (i.e., stress distribution at monitoring line 2). The advance stress concentration zone was roughly distributed in the middle and on the right uncut side. Noted that there is a clear stress reduction area near the roof cutting seam. The transverse range of the stress reduction zone was approximately 30 cm, 15 m in actual mining condition, which will be more conducive to the safe operation of the working face and the stability of the retained roadway.

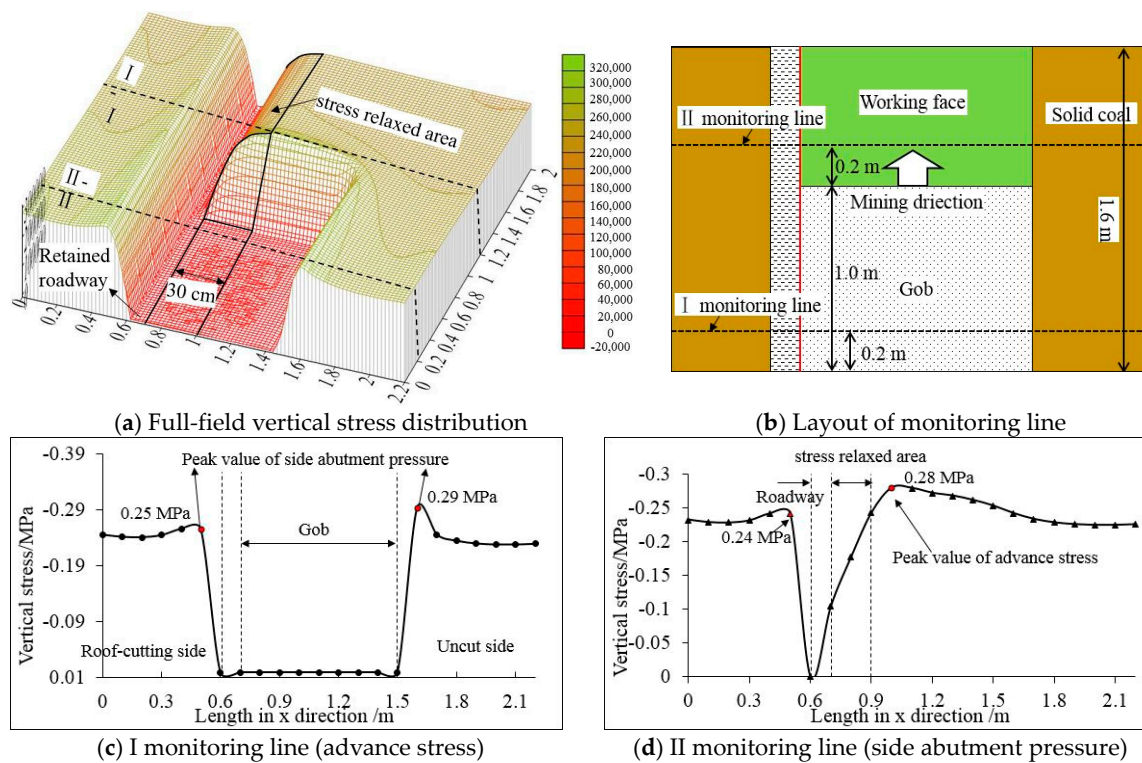
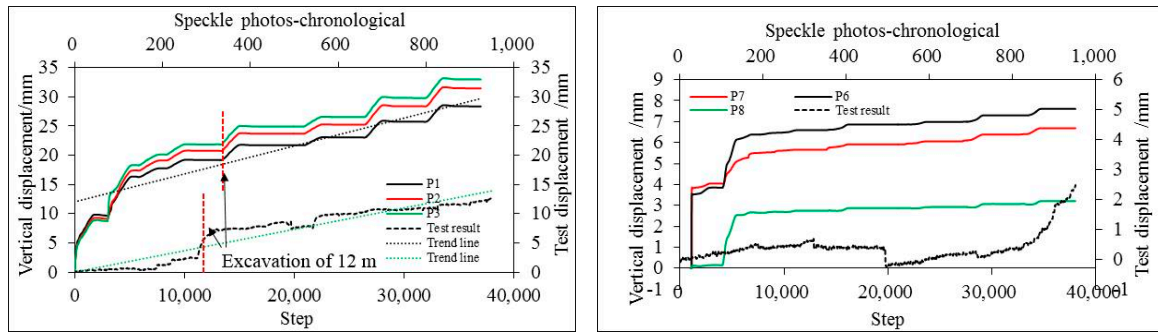


Figure 19. Stress distribution in stope.

### 5.2.3. Analysis of the Retained Roadway Deformation

Figure 20a,b show the displacement time–history curve of the roadway roof and floor monitoring points. The measuring points were the same as those in the model test. The dotted line represents the simulated data results, while the implementation represents the model test results. Figure 20a also illustrates that the roof displacement curves underwent a rapid deformation before the working face was excavated for 24 cm, i.e., 12 m in actual situation and became relatively stable after that. That is, the farther the monitoring point from the working face, the smaller the roof deformation rate. The roof deformation can be divided into the rapid and stable deformation stages. The variation trend was similar to that of the model test, but a certain difference existed between the deformation values of the two. The support effect was not considered in the simulation; thus, the deformation value was large. The deformation value of roadway in the model test is relatively accurate, with the maximum roof deformation value of 14 mm and the maximum floor deformation value of 4 mm. By multiplying the similar geometric ratio, known that the actual deformation amount of roof is 21 cm and the maximum floor deformation amount is 6 cm, these deformation values are relatively small and safe in the field construction. Regardless of the type of investigation (numerical simulation or field test), the displacement change law of the solid coal measuring points was relatively stable, and the deformation value was small.

By calculating the numerical model with the same size as that in the model test and extracting the displacement data of the same location for a comparative analysis, we can conclude that the deformation values of the two had certain errors, but the overall deformation law was relatively similar. The value of the mechanical parameters of each lithology of the numerical model was reasonable and helped explain the rationality of the model test.



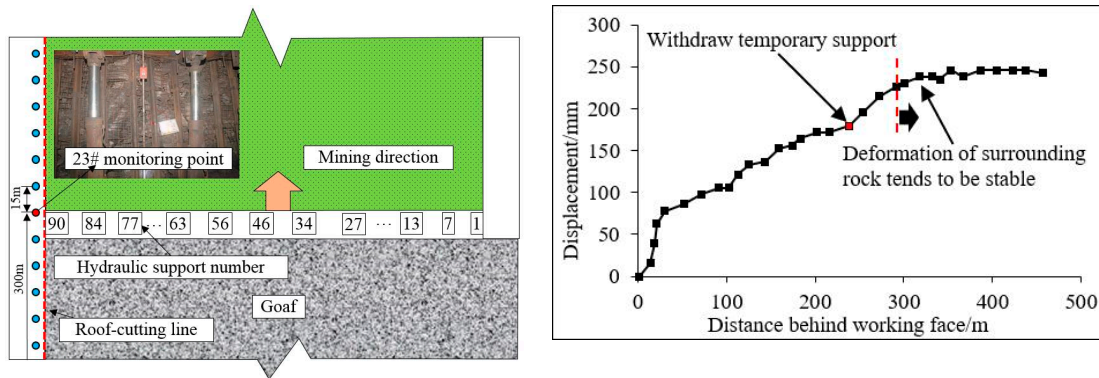
(a) Vertical displacement of roof (b) Horizontal displacement of solid coal

Figure 20. Deformation curve of surrounding rock.

6. On-Site Monitoring

6.1. Roof Deformation Monitoring

Through the analysis of the model test and numerical simulation, the laws of rock strata movement and the deformation laws of roadway preliminarily summarized. It is proposed to combine with field monitoring to further study the deformation law. Figure 21 shows the arrangement of measuring points and roof subsidence curve, when the working face advances to point 23, the monitoring begins. It shows that the deformation rate is larger within 30 m behind the working face, which indicates that the influence of mining dynamic pressure is more intense in this stage, and then further away from the working face, the roof subsidence tends to be gentle; the overall trend is similar to the test and simulation curve.



(a) Arrangement of measuring points (b) 23# measuring point displacement curve

Figure 21. Roof displacement monitoring.

6.2. Mine Pressure Monitoring

Figure 21a shows the number of hydraulic support. Figure 22 shows the stress monitoring curve of the working face hydraulic support (88#) on the roof cutting side. The curve can be divided into two sections: (1) 0–220 m traditional GSER section and (2) 220–600 m roof cutting section. The stress of the hydraulic support decreased when the new GSER was adopted. Moreover, the maximum value decreased from 66.7 MPa to 57.2 MPa, which is 14.2% lower. The average stress decreased from 44.3 MPa to 37.5 MPa, which is 15.3% lower. In other words, the stress of the support on the roof cutting side is effectively reduced by the roof cutting, which is beneficial to the safe operation of the working face and optimizes the stress distribution of the retained roadway surrounding rock. The stress reduction zone caused by the roof cutting was verified in the numerical simulation.

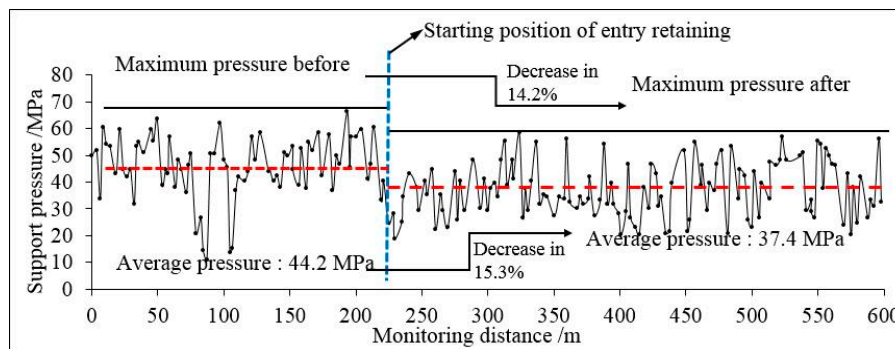


Figure 22. Working face pressure.

## 7. Conclusions

Despite the wide application of GSER by roof cutting, only a few fundamental studies focused on the movement law of the overlying strata and the deformation characteristics of roadways. In this study, we used theoretical analysis, model testing, and numerical simulation to reach the following conclusions:

1. A structural model of the roadway surrounding rock was developed. The simplified cantilever beam mechanical model was established, and the deformation equation of the roof was derived to show that the deflection deformation was the largest on the roof cutting side.
2. The model test results showed that in the early stage of the strata movement, the rock mass at the roof cutting side collapsed first, and the displacement was larger than that of the uncut side. In the later stages, the subsidence displacement of the strata within the height range of the roof cutting was asymmetrically distributed. The displacement was smaller further away from the cutting seam. Outside of the roof cutting height, the bending fracture of the rock layer was virtually unaffected. The displacement curve gradually formed a symmetrical distribution as the distance from the working face increased.
3. Based on the FLAC3D simulation, the subsidence law of the overlying strata was consistent, although the simulated value was smaller than the measured value. The reason for this is that the compression deformation of the whole model was considered in the physical test. The result of the displacement monitoring of the retained roadway indicated that the simulated value was larger mainly because the roadway in the model test had supporting measures, but the supporting effect was not considered in the numerical simulation.
4. The field monitoring results showed a strong influence of the mining dynamic pressure on the retained roadway roof within 30 m behind the working face with a large displacement deformation rate. Farther from the working face, the displacement deformation rate stabilized. The average stress of the hydraulic support near the retained roadway decreased from 44.3 MPa to 37.5 MPa after the roof cutting (i.e., 15.3% decrease). The pressure was effectively reduced by the roof cutting, thereby forming a stress reduction area. These results will help future mining operations optimize roof cutting designs for a safe and efficient operation and provide analytical models and tools for future supplemental studies.

**Author Contributions:** Writing and original draft preparation: D.Z. and Z.S.; methodology: W.G.; formal analysis: J.W.; investigation: J.W.; and software: D.Z. and J.W. All authors have read and agreed to the published version of the manuscript.

**Funding:** The work was financially supported by the National Natural Science Foundation of China (No. 51574248) and the National Key Research and Development Program (No. 2016YFC0600901).

**Acknowledgments:** The authors also express their gratitude for the support from the State Key Laboratory for Geomechanics and Deep Underground Engineering, China University of Mining and Technology (Beijing).

**Conflicts of Interest:** The authors declare no conflict of interest.

## References

1. Azadeh, A.; Osanloo, M.; Ataei, M. A new approach to mining method selection based on modifying the Nicholas technique. *Appl. Soft Comput.* **2010**, *10*, 1040–1061. [[CrossRef](#)]
2. Ghasemi, E.; Ataei, M.; Shahriar, K. An intelligent approach to predict pillar sizing in designing room and pillar coal mines. *Int. J. Rock Mech. Min. Sci.* **2014**, *65*, 86–95. [[CrossRef](#)]
3. He, M.C.; Xie, H.P.; Peng, S.P.; Jiang, Y.D. Study on rock mechanics of deep mining. *Chin. J. Rock Mech. Eng.* **2005**, *16*, 2803–2813.
4. Lollino, P.; Martimucci, V.; Paris, M. Geological survey and numerical modeling of the potential failure mechanisms of underground caves. *Geosyst. Eng.* **2013**, *16*, 100–112. [[CrossRef](#)]
5. Bai, J.B.; Zhou, H.Q.; Hou, C.J.; Tu, X.Z.; Yue, D.Z. Development of side support technology for gob side entry retaining. *J. China Univ. Min. Technol.* **2004**, *2004*, 59–62.
6. He, M.C.; Gao, Y.B.; Yang, J.; Gong, W.L. An Innovative Approach for Gob-Side Entry Retaining in Thick Coal Seam Longwall Mining. *Energies* **2017**, *10*, 1785. [[CrossRef](#)]
7. Wang, Q.; Jiang, B.; Pan, R.; Li, S.C.; He, M.C.; Sun, H.M.; Qin, Q.; Yu, H.C.; Luan, Y.C. Failure mechanism of surrounding rock with high stress and confined concrete support system. *Int. J. Rock Mech. Min. Sci.* **2018**, *102*, 89–100. [[CrossRef](#)]
8. Wang, Q.; He, M.C.; Yang, J.; Gao, H.K.; Jiang, B.; Yu, H.C. Study of a no-pillar mining technique with automatically formed gob-side entry retaining for longwall mining in coal mines. *Int. J. Rock Mech. Min. Sci.* **2018**, *110*, 1–8. [[CrossRef](#)]
9. Sun, X.M.; Liu, X.; Liang, G.F.; Wang, D.; Jiang, Y.L. Study on key parameters of thin coal seam roof cutting and pressure relief gob side entry retaining. *J. Rock Mech. Eng.* **2014**, *33*, 1449–1456.
10. Wang, P.; Jiang, L.S.; Li, X.Y.; Qin, G.P.; Wang, E.Y. Physical Simulation of Mining Effect Caused by A Fault Tectonic. *Arab. J. Geosci.* **2018**, *11*, 741. [[CrossRef](#)]
11. Gao, Y.B.; Wang, Y.J.; Yang, J.; Zhang, X.Y.; He, M.C. Meso- and macroeffects of roof split blasting on the stability of gateroad surroundings in an innovative nonpillar mining method. *Tunn. Undergr. Space Technol.* **2019**, *90*, 99–118. [[CrossRef](#)]
12. Wang, Y.J.; Gao, Y.B.; Wang, E.Y.; He, M.C.; Yang, J. Roof deformation characteristics and preventive techniques using a novel non-pillar mining method of gob-side entry retaining by roof cutting. *Energies* **2018**, *11*, 627. [[CrossRef](#)]
13. Guo, Z.B.; Wang, Q.; Wang, H.H.; Ma, Z.M.; Yin, S.Y.; Hu, H.L. Analysis of the swelling characteristics and lateral pressure of the mudstone in the rubble side of the cut top Lane. *J. China Univ. Min. Technol.* **2018**, *47*, 987–994.
14. Jiang, L.S.; Wang, P.; Zheng, P.Q.; Luan, H.J.; Zhang, C. Influence of Different Advancing Directions on Mining Effect Caused by a Fault. *Adv. Civ. Eng.* **2019**, *2019*, 1–16. [[CrossRef](#)]
15. Kang, H.P.; Niu, D.L.; Zhang, Z.; Lin, J.; Li, Z.H.; Fan, M.J. Deformation characteristics and support technology of surrounding rock in deep gob side entry retaining. *Chin. J. Rock Mech. Eng.* **2010**, *29*, 1977–1987.
16. Lee, Y.J.; Bassett, R.H. Application of a photogrammetric technique to a model tunnel. *Tunn. Undergr. Space Technol.* **2006**, *21*, 79–95. [[CrossRef](#)]
17. Pan, B.; Qian, K.M.; Xie, H.M.; Asundi, A. Two-dimensional digital image correlation for in-plane displacement and strain measurement: A review. *Meas. Sci. Technol.* **2020**, *20*, 062001. [[CrossRef](#)]
18. Abanto-Bueno, J.; Lambros, J. Investigation of crack growth in functionally graded materials using digital image correlation. *Eng. Fract. Mech.* **2002**, *69*, 1695–1711. [[CrossRef](#)]
19. Zhu, W.S.; Zhang, Q.B.; Zhu, H.H.; Li, Y.; Yin, J.H.; Li, S.C.; Sun, L.F.; Zhang, L. Large-scale geomechanical model testing of an underground cavern group in a true three-dimensional (3-D) stress state. *Can. Geotech. J.* **2010**, *47*, 935–946. [[CrossRef](#)]
20. Wang, P.; Jiang, L.S.; Zheng, P.Q.; Qin, G.P.; Zhang, C. Inducing-modes analysis of rock burst in fault-affected zone with a hard thick stratum occurrence. *Environ. Earth Sci.* **2019**, *78*, 467. [[CrossRef](#)]
21. Zhang, N.; Han, C.L.; Yi, J.G.; Zheng, X.G. Theory and practice of surrounding rock control in gob side entry retaining. *J. Chin. Coal Soc.* **2014**, *39*, 1635–1641.
22. Yamamoto, K.; Kusuda, K. Failure mechanisms and bearing capacities of reinforced foundations. *Geotext. Geomembr.* **2001**, *19*, 127–162. [[CrossRef](#)]

23. Sterpi, D.; Cividini, A. A physical and numerical investigation on the stability of shallow tunnels in strain softening media. *Rock Mech. Rock Eng.* **2004**, *37*, 277–298. [[CrossRef](#)]
24. Seki, S.; Kaise, S.; Morisaki, Y.; Azetaka, S.; Jiang, Y. Model experiments for examining heaving phenomenon in tunnels. *Tunn. Undergr. Space Technol.* **2008**, *23*, 128–138. [[CrossRef](#)]
25. Ghabraie, B.; Ren, G.; Smith, J.; Holden, L. Application of 3D laser scanner, optical transducers and digital image processing techniques in physical modelling of mining-related strata movement. *Int. J. Rock Mech. Min. Sci.* **2015**, *80*, 219–230. [[CrossRef](#)]
26. Li, Z.K.; Liu, H.; Dai, R.; Su, X. Application of numerical analysis principles and key technology for high fidelity simulation to 3-D physical model tests for underground caverns. *Tunn. Undergr. Space Technol.* **2005**, *20*, 390–399. [[CrossRef](#)]
27. Indraratna, B.; Nemcik, J.A.; Gale, W.J. Review and interpretation of primary floor failure mechanism at a longwall coal mining face based on numerical analysis. *Geotechnique* **2000**, *50*, 547–557. [[CrossRef](#)]



© 2020 by the authors. Licensee MDPI, Basel, Switzerland. This article is an open access article distributed under the terms and conditions of the Creative Commons Attribution (CC BY) license (<http://creativecommons.org/licenses/by/4.0/>).